RESEARCH ARTICLE | OCTOBER 10 2024

Lagrangian particle tracking at large Reynolds numbers

Christian Küchler ; Antonio Ibanez Landeta ; Jan Moláček ; Eberhard Bodenschatz

Rev. Sci. Instrum. 95, 105110 (2024)
https://doi.org/10.1063/5.0211508

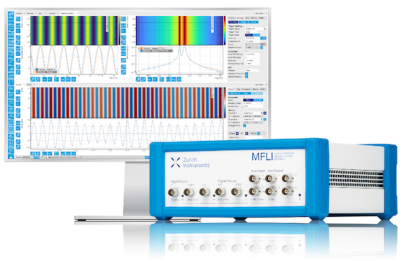

Review of Scientific Instruments ARTICLE pubs.aip.org/aip/rsi

Lagrangian particle tracking at large Reynolds numbers

Cite as: Rev. Sci. Instrum. 95, 105110 (2024); doi: 10.1063/5.0211508
Submitted: 31 March 2024 • Accepted: 24 September 2024 •
Published Online: 10 October 2024

Christian Küchler,[1] Antonio Ibanez Landeta,[1] Jan Moláček,[1] and Eberhard Bodenschatz[1,2,a)]

AFFILIATIONS

[1] Max-Planck-Institute for Dynamics and Self-Organisation, 37077 Göttingen, Germany
[2] Cornell University, Ithaca, New York 14853, USA

[a)] **Author to whom correspondence should be addressed:** eberhard.bodenschatz@ds.mpg.de

ABSTRACT

In the study of fluid turbulence, the Lagrangian frame of reference represents the most appropriate methodology for investigating transport and mixing. This necessitates the tracking of particles advected by the flow over space and time at high resolution. In the past, the purely spatial counterpart, the Eulerian frame of reference, has been the subject of extensive investigation utilizing hot wire anemometry that employs Taylor's frozen flow hypotheses. Measurements were reported for Taylor scale Reynolds number $R_\lambda > 10^4$ in atmospheric flows, which represent the highest strength of turbulence observed on Earth. The inherent difficulties in accurately tracking particles in turbulent flows have thus far constrained Lagrangian measurements to Taylor scale Reynolds numbers up to approximately $R_\lambda = 10^3$. This study presents the Lagrangian particle tracking setup in the Max Planck Variable Density Turbulence Tunnel (VDTT), where Taylor scale Reynolds numbers between 100 and 6000 can be reached. It provides a comprehensive account of the imaging setup within the pressurized facility, the laser illumination, the particles used, and the particle seeding mechanism employed, as well as a detailed description of the experimental procedure. The suitability of KOBO Cellulobeads D-10 particles as tracers within the VDTT is illustrated. The results demonstrate that there is no significant charge exhibited by the particles and that the impact of their inertia on the results is negligible across a wide range of experimental conditions. Typical data are presented, and the challenges and constraints of the experimental approach are discussed in detail.

I. INTRODUCTION

Turbulence can be described both in the stationary Eulerian reference frame, i.e., by studying snapshots of vector fields, or in the co-moving Lagrangian reference frame of a material element.[1] While measurements in the Eulerian frame of reference have been performed routinely since the early 1900s,[2] Lagrangian measurements at very high turbulence levels remain the utmost challenge. The turbulence level is best compared across experiments by the Taylor-scale Reynolds number ($R_\lambda = u\lambda/\nu$), where u is the standard deviation of the velocity, λ is the Taylor microscale, and ν is the kinematic viscosity of the fluid. Reynolds numbers $R_\lambda > 5000$ have been reported both in laboratory experiments[3–6] and in the atmosphere,[7,8] but measurements were restricted to (mostly one-dimensional) Eulerian quantities. In the atmosphere, large-scale particle tracking has been performed (e.g., Ref. 9), but the particles were about 25× larger than the smallest flow scales and, therefore, too large to perform fundamental studies on turbulent flows. Bertens *et al.*[10] studied the motion of cloud droplets of varying size at $R_\lambda \sim 3000$. In the laboratory, setups without a mean flow are preferred for fundamental Lagrangian studies since they allow particles to remain in view for a long time. Particularly large turbulence levels of $R_\lambda \approx 1000$ have been achieved using the von-Kármán-setup of two counter-rotating disks inside a water tank by Mordant *et al.*[11] and Ouellette *et al.*[12] Saw *et al.*[13] reached $R_\lambda = 660$ in an air-filled wind tunnel with an active grid to study the clustering of inertial particles. Laboratory setups studying Lagrangian turbulence at R_λ exceeding 1000 or adequate atmospheric studies are not known to the authors. Large Reynolds numbers are desirable because they are known to reveal universal properties of turbulent flows that are obscured by viscous effects at lower Reynolds numbers. In the Lagrangian reference frame, viscous effects diminish slower with increasing R_λ, making large Reynolds numbers even more relevant than in the Eulerian reference frame.[14]

Within the Eulerian perspective, for 3D incompressible fluid turbulence, the statistics of turbulent velocity fluctuations can be understood by the transfer of kinetic energy from large to small spatial scales with a rate ε (power per unit mass). At the small spatial scales, this energy is dissipated into heat. ε is called the energy dissipation rate. The largest flow length- and time scales (L and T_L, respectively) are given by the energy injection mechanism, whereas the fluid viscosity ν determines the dynamics at the viscous energy dissipating (Kolmogorov) scales η and τ_η, respectively. In the Lagrangian frame, even for a Taylor-scale Reynolds number $R_\lambda = 2000$, which is considered large for the Eulerian frame, the separation in temporal scales is only $T_L/\tau_\eta \approx 300$. Therefore, to this date there is little knowledge on Lagrangian properties of fully developed turbulence in experiments and idealized numerical simulations, with the most significant one being acceleration statistics of Lagrangian tracers.[15]

Lagrangian measurements rest on the tracking of small particles chosen to follow the fluid material elements as passive tracers. From these tracks, the local flow velocity **u** and acceleration **a** can be inferred. The particles' ability to respond to a given change in the fluid motion is given by their response time,[16–18]

$$\tau_p = \frac{1}{18} d^2 \frac{(\rho_P - \rho_F)}{\nu_F \rho_F}, \tag{1}$$

where d is the particle diameter, ρ_P and ρ_F the particle- and fluid densities, respectively, and ν_F is the kinematic viscosity of the fluid. This response time is compared to the viscous time scale τ_η to yield the Stokes number $\mathrm{St} = \tau_p/\tau_\eta$, which characterizes the particles' ability to follow a given turbulent flow. In order to relate the particles' velocity and acceleration to those of the flow, the particle size should furthermore not significantly exceed the viscous (Kolmogorov) length scale of the turbulence.[17]

Common tracer particles for water flows include polystyrene particles.[16,17] In gaseous flows, droplets of vegetable oil or glycol–water solutions, particularly small solid particles of TiO_2,[19] and helium-filled soap bubbles have been options. The latter are relatively large and, therefore, easy to visualize, while the helium reduces their mean density close to that of air. Particles can also be "designed" to allow for local measurements of flow quantities, such as vorticity[20] or the entire velocity gradient tensor.[21]

In flow diagnostics, particles are typically illuminated using high-intensity pulsed laser beams, such that even particles with a very small surface area scatter enough light to be detected by commercial cameras. Note that choosing very small particles to obtain a fast particle response time τ_p reduces the amount of scattered light and increases the illumination requirements. It is thus advantageous to optimize $\rho_p - \rho_F$ in Eq. (1), e.g., by using larger but lighter particles (with the associated small Stokes number). Particles should not be larger than the Kolmogorov scale η of the turbulence, as they should not average the flow due to their size. Recently, light-emitting diode arrays have been assembled to deliver less hazardous illumination at reduced costs.[22,23] Another alternative is fluorescent[24] or phosphorescent[25] particles, which can reduce the demands on the light source intensity at the expense of a very limited selection of particles.

The imaging device is the central limiting factor in any particle tracking setup, which must first and foremost be fast enough in terms of Kolmogorov times (>10 frames/τ_η).[17,26] The relatively small amount of light scattered by a single particle furthermore demands a very sensitive sensor. The optical elements must then be chosen such that a single particle image (particle projection and optical aberrations) spans at least two pixels to achieve sub-pixel positioning precision.[26,27] The first 3D-optical measurements of fully developed Lagrangian turbulence at high Reynolds numbers were recorded on silicon-strip detectors from high-energy physics.[16,17,28] While CCD camera sensors permit Lagrangian particle tracking only at moderate Reynolds numbers,[29] the large number of readout channels on CMOS sensors enable frame rates of up to 25 Gpx/s in commercial high-speed cameras.[30,31] It is important to note that for 3D measurements, three to four cameras are needed for stereoscopic imaging.[26,29,32] The rapid permanent storage of this massive stream of data is time-consuming in practice and a field of active industrial development efforts. An alternative to the conventional imaging of particle tracks is digital holography.[33] This has the advantage of requiring only one camera while allowing for larger particle densities and particle sizing.

To obtain long particle tracks, it is advantageous to remove any mean motion of the particles across the limited field of view. Hence, most Lagrangian experiments are performed in flows without a mean flow, such as von-Kármán mixers[16,26,34] or specially designed turbulence generators.[35,36] In wind- and water tunnels, the camera and illumination systems are placed on carriages that move at the mean flow speed,[37] or the length of the particle tracks is sacrificed in simpler stationary setups.[38]

A wide range of software packages have been developed that allow the frame-by-frame tracking of imaged particles and the subsequent transformation of two-dimensional pixel coordinates to three-dimensional "world" coordinates. The conventional method is to employ a predictor-corrector scheme[26,30,39,40] and a triangulation based on the simple pinhole camera model.[41] The recent shake-the-box algorithm[42] allows much larger particle densities on the images, makes particle identification more efficient, and performs better overall. Recently, an open source code based on the shake-the-box algorithm has been made available.[43] For a recent review of particle tracking schemes, we refer the reader to Schröder and Schanz.[32]

At large Reynolds numbers, Lagrangian fluctuations occur over a wide range of time scales. Small particles move vigorously on small time scales, while the tracks remain statistically correlated for long times. Capturing these rich motions by imaging is challenging because small particles need to be followed over long times and potentially long distances while measuring their spatiotemporal location at high resolution.

This article presents a solution to the aforementioned problem in the form of a stationary Lagrangian particle tracking system in a high-pressure, active-grid driven wind tunnel flow. Specifically, it considers the Variable Density Turbulence Tunnel (VDTT), which employs compressed gaseous SF_6.[3] First, the most significant features and modifications of the VDTT are given, and a critical analysis of the advantages and disadvantages of SF_6 as a working fluid is presented. Subsequently, the article describes the KOBO Cellulobeads D-10 particles selected for use and the dispersion mechanism employed. It then explains the laser illumination and camera setup, as well as the particle tracking code developed in-house and the initial measurements taken to demonstrate the successful operation of the experiment. Finally, it examines the

overall capabilities of the setup. It is shown that particle charge, while present, is negligible and that particle inertia is sufficiently small to allow faithful fluid element tracking. Exemplary measurements of the Lagrangian second order structure function and of acceleration statistics are presented.

II. PARTICLE TRACKING IN THE MAX-PLANCK VARIABLE DENSITY TURBULENCE TUNNEL

Generating large Reynolds numbers in approximately statistically homogeneous and isotropic laboratory flows has challenged the scientific community for decades (see above). The Göttingen Max-Planck Variable Density Turbulence Tunnel (VDTT) solves this problem in a particularly flexible manner. It has been described in detail in Bodenschatz *et al.*,[3] where complete specifications can be found. Here only a brief introduction is given; so far, it is important for the work presented here. The VDTT uses the heavy gas SF_6 at pressures up to 15 bar, thereby increasing the density ρ while keeping the dynamic viscosity of the gas unaltered. Therefore, the kinematic viscosity $\nu = \mu/\rho$ is very small, and since $R_\lambda \sim 1/\nu$, the Reynolds numbers can be made large by increasing the pressure, i.e., the density of the gas. Please note that SF_6 is non-corrosive and non-toxic but is a strong greenhouse gas, and emissions into the atmosphere must be kept at a bare minimum.

The VDTT is a closed-loop wind tunnel and reaches mean flow speeds between 0.5 and 5.5 m/s. The measurement section is shown schematically in Fig. 1. The flow enters the measurement section through an active grid with individually controlled winglets.[44,45] A schematic of the active grid is shown in Fig. 2.

This active grid is more flexible than traditional passive grids of rigid bars and allows us to reach about 5× higher Reynolds numbers than a passive grid.[46] It consists of 111 motorized winglets (11×11 cm^2), whose angle with respect to the mean flow can be individually adjusted over 180° at a speed of up to 40° per 0.1 s. By correlating these angles in space and time, the blockage of the tunnel cross section can be controlled locally and dynamically. It has been shown that this type of active grid can generate correlated fluid structures of variable size[44] while maintaining an adequate shear-free central region.[47] This homogeneous region can be expanded by systematically reducing the active grid blockage of the active grid flaps close to the wall. Most importantly, the active grid allows for a fine control of the length scale where turbulent kinetic energy is injected into the flow and thereby the Reynolds number. It needs to be emphasized here that the variable density aspect of the wind tunnel allows us to adjust the Reynolds number not only by adjusting the energy injection scale or the fluctuating velocity but also by adjusting the pressure and thereby the kinematic viscosity.

In terms of measurement flexibility, this allows for detailed investigations of finite-resolution effects since the same Reynolds number can be reached by adjusting mean flow speed, active grid protocol, and kinematic viscosity.[45,47,48] Bringing together control over the smallest length scales through density (i.e., pressure) and control over the largest scales through the active grid results in the aforementioned parameter flexibility and large yet unsurpassed Reynolds numbers at low mean flow speeds, which are ideal for particle tracking measurements.[3]

It has been shown[49] that the turbulent kinetic energy decays downstream of the active grid, while its integral length scale defined as $L = \int \langle u(x) \cdot u(x+r) \rangle dr$ remains approximately constant. This

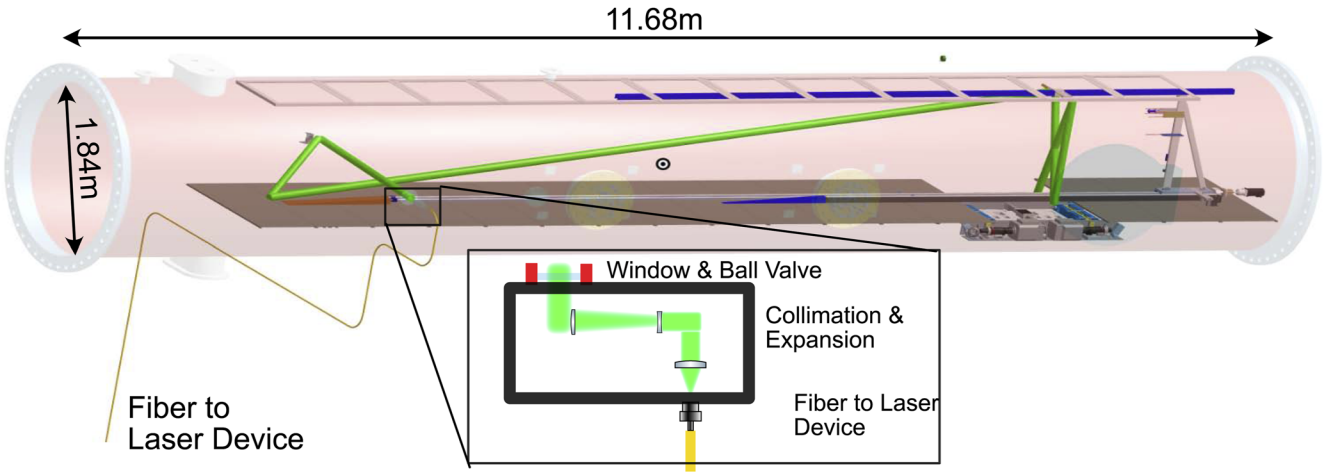

FIG. 1. Schematic of the measurement section of the wind tunnel. The active grid and particle dispenser were located at the left of the tunnel's bottom cover, and the flow was from left to right. Green laser light from a Yb:YLF-laser was guided toward an optics box through an optical fiber. The diverging beam was collimated and expanded through lenses. It entered the tunnel as an ~3.5 cm wide beam with minimal divergence. The beam was guided toward the opposite end of the measurement section, where an arrangement of three mirrors formed an "X" with the measurement volume in its joint. The cameras resided below the measurement section floor and observed the measurement volume through optical windows. The particle tracking measurement volume was located 7 m downstream of the active grid, 54–58 cm above the floor, and in the center of the 1.5 m wide measurement section. An 8 cm wide traverse was located ~1.3 m downstream of the measurement volumes, with hot wires protruding about 20 cm for highly resolved stream-wise velocity measurements.

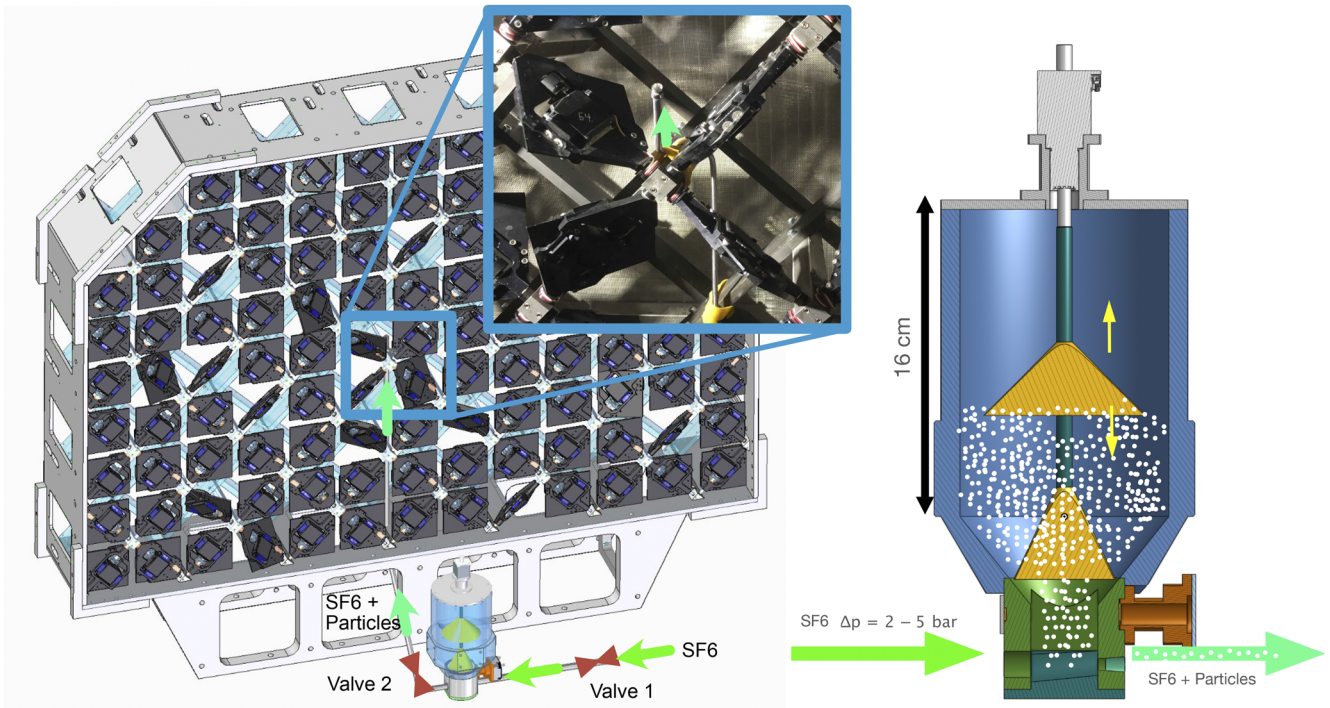

FIG. 2. Active grid and particle dispersion. An external SF_6 supply (3–5 bar above facility pressure) was connected to the particle reservoir, where the gas flow collected particles. The reservoir was pressurized upon opening valve 1 (located outside the wind tunnel), and the gas flow was started by opening valve 2. The particles were released through a 0.5 mm aperture nozzle. The particles traveled ~2 m inside the pipes. The flaps had a side length of 0.11 m for reference of scale.

indicates that the turbulence decay is influenced by the finite size of the measurement section.

The VDTT challenges flow measurements: the viscous length- and time scales are small, i.e., $\eta > 10$ μm and $\tau_\eta > 0.1$ ms, respectively. Therefore, small particles with a fast response time are required (see below). Consequently, the camera tracking system must have high frame rates and, in addition, must have high spatial resolution. At the same time, the illumination must be sufficiently bright for particles to be imaged at the small exposure times required. Furthermore, the refractive index n of SF_6 changes sensitively with pressure and temperature.[50] For example, an increase in pressure from 10 to 11 bar changes n by 0.008 in SF_6, but by only 0.0003 in air.[51] In SF_6 at 10 bars, a temperature change of 1 K leads to a change in the refractive index of SF_6 comparable to that of a 200 K increase in air at standard pressure. Hence, the line-of-sight of the cameras cannot contain large temperature gradients, and all focal lengths must be remote-controllable to account for changes in the facility pressure. The camera calibration must equally be based on a remote-controlled system that can be brought into and removed from the camera's field of view. All these challenges were met in the experiments presented here and are discussed in detail below.

III. PARTICLES AND THEIR DISPERSION

We measured the turbulent flow with KOBO Cellulobeads D-10 as tracers. These are cellulose particles and typically serve as a primary product for the cosmetics industry, where they are used to diffusely scatter light. They have been designed to be biologically degradable and, therefore, pose only minimal health risks. This is in contrast to other solid particles used to seed turbulent flows, such as hollow glass spheres, TiO_2, or polystyrene particles. Cellulobeads are flammable and in the air can lead to dust explosions. In an SF_6 atmosphere, this is not an issue since the gas is inert.

In order for the particles to be faithful tracers of fluid elements, the Stokes number $St = \tau_p/\tau_\eta$ must be small. We now detail the methods we used to estimate St. The particle radius a is straightforward to measure using microscopic images of single particles as described below. The fluid density and viscosity are well known.[52] To calculate the particle response time τ_p, the particle density must be measured. For this, we repurpose a TSI Aerodynamic Particle Sizer Model 3321 (APS), which directly measures the particle response time through a time-of-flight technique and infers the particle diameter from a pre-defined particle density. The aerodynamic particle size is then given by[53]

$$d_{ae} = 2a\sqrt{F\frac{\rho_p}{\rho_{Ref}}}, \tag{2}$$

where ρ_{Ref} is a device-specific reference density and F is a shape factor taking into account differences in fluid response for different particle shapes. Since the KOBO Cellulobeads D-10 were spherical, their shape factors are taken as $F = 1$. Comparing the APS output diameter with the geometric diameter $2a$ yielded a measure for the

particle density. Figure 3(b) shows a distribution of the particle density calculated in this way. The grayed-out part of the plot is likely due to contamination from a previous experiment. The relevant part shows a relatively wide distribution of particle densities, from which we estimated $\rho_p = (730 \pm 250)$ kg/m^3. This density is half the nominal density of cellulose,[54] indicating that the particles contained voids.

In combination, the measurements of a and ρ_p allow for an estimate of the Stokes numbers to be expected for different flow parameter settings. Figure 3(c) shows the Stokes number for different values of the facility pressure and the turbulence dissipation rate. Only at small pressures or dissipation rates was the Stokes number below 0.1. The flexibility of the VDTT allowed us to change the Stokes number while keeping the Reynolds number constant. This is illustrated in Fig. 2(d), where we show the parameter space of St and R_λ spanned by the facility when using Cellulobeads D-10 particles as tracers. By using larger Cellulobeads, an even wider range of Stokes numbers could be investigated. This was not conducted here, as the aim of this investigation is to study passive tracers. Using smaller Cellulobeads would be advantageous in terms of small Stokes numbers, but this would require an even more powerful lighting system. As in this experiment, we already used a 300 W high repetition laser; brighter light sources were not available to us (see also below).

The particles were injected into the wind tunnel flow using an in-house particle dispenser depicted in Fig. 2. It consisted of a reservoir (blue) and a smaller cavity (green) connected to an external SF_6 supply and a nozzle through flexible metallic pipes. For each experiment, a portion of the particles fell into the cavity and were washed away by a flow of SF_6 toward the nozzle, where the fluid shear forces broke up agglomerates to form a cloud of mostly mono-disperse particles (see Fig. 3). The number of particles within the cavity could not be controlled precisely, which caused most of the variation in the seeding density apart from the wind tunnel turbulence itself.

The SF_6 supply was a conventional gas bottle with a pressure regulator. The pressure regulator was set to 2–5 bar above the tunnel's pressure, which is one means of influencing the seeding density in the measurement volume. Since the particle dispenser itself was not free of leaks, the gas supply was interrupted between experiments through a magnetically actuated valve. A second magnetically actuated valve at the outlet of the dispenser controlled the flow of SF6 and with it the subsequent release of particles through the nozzle. The opening time was used as the second means of controlling the seeding density. The nozzle was a 1.2 mm Laval nozzle removed from a commercial airbrush. All parts of the particle dispenser were carefully electrically grounded, and the ground connection is verified whenever the setup is adjusted.

The ejection nozzle was placed between flaps of the active grid 15 cm left of the measurement section centerline at the

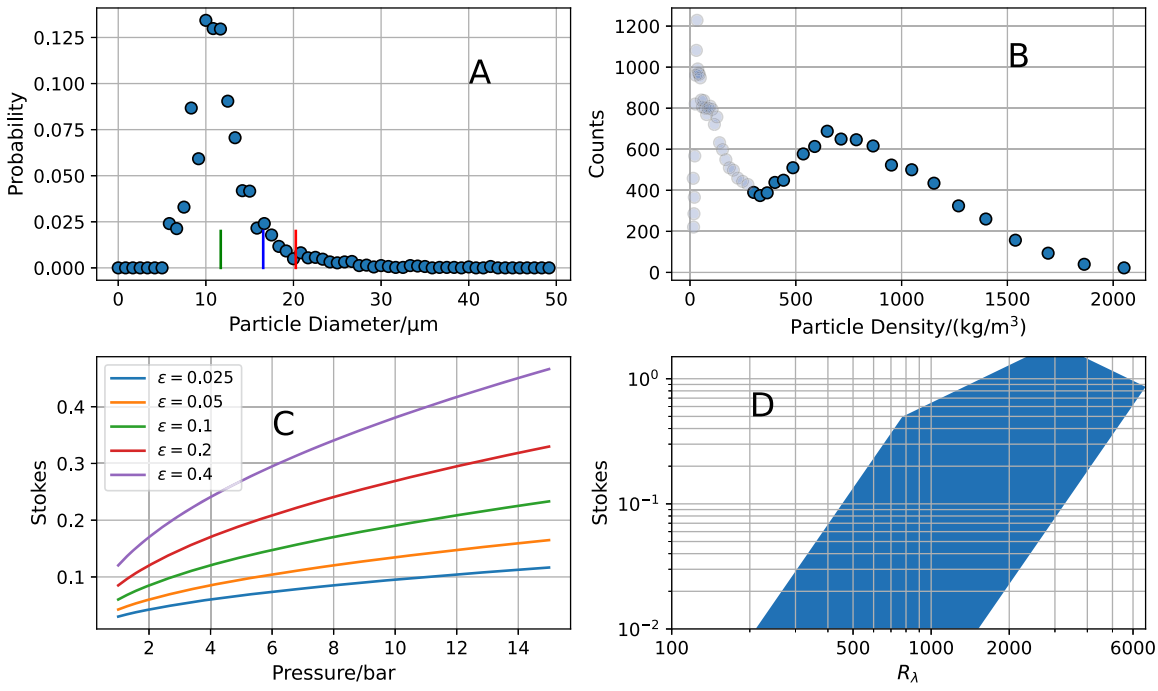

FIG. 3. (a) Probability distribution of particle sizes determined from microscopic images of settled particles. Colors indicate expected values for clusters of one (green), two (blue), or three (red) particles. The mean particle diameter in the green sector is (11.7 ± 0.1) μm. (b) Histogram of the particle density estimated from the particle response time to a calibrated fluid acceleration. The peak around 2.5 μm is likely a residual from a previous experiment. From this distribution, we estimate the effective particle density and its error as $\rho_p = 730$ kg/m^3. (c) Estimate of the Stokes number using the values of particle diameter and density along with known fluid and turbulence properties. (d) Range of Stokes numbers obtainable at given R_λ. St < 0.1 can only be reached for $R_\lambda < 3000$.

upstream end of the measurement section. The nozzle pointed about 40° upward. This ensured that the seeded portion of the flow was dominated by the approximately homogeneous and isotropic active grid turbulence instead of the jet ejecting the particles. It furthermore homogenized the seeding density.

Within the reservoir, two metallic cones (yellow) were connected to a stepper motor, which moved them vertically. This mechanism allowed for remote declogging of the device, but its usage was very rarely required, likely due to the frequent short flows of SF_6. We achieved seeding densities of up to 130 particles/cm^3 and ejected an estimated 0.1 ml of particles per recorded video.

We verified that the particle dispenser released predominantly single particles. For this, we had placed a microscope slide on the floor of the measurement section during experiments. The ejected particles settled onto this slide, and their size distribution was measured using microscopic images and ImageJ-based particle sizing. Figure 3(a) shows that predominantly single particles with a narrow size distribution were ejected.

Pneumatic conveyance as was implemented here is known to electrostatically charge the conveyed particles. To assess the effect of the electrical charge of the particles on the flow measurement, we followed two approaches: First, we measured the radial distribution function (RDF) of the particles, i.e., the relative probability of finding a particle a distance r away from another. The RDF of electrostatically repelling particles in a turbulent flow differs from the RDF of uncharged particles[56,57] for distances r where the electrostatic forces exceed the fluid forces. Second, we calculated the vectorial difference between the accelerations of two adjacent particles $\boldsymbol{\delta a} = \mathbf{a_1} - \mathbf{a_2}$ separated by $\boldsymbol{\delta r} = \mathbf{r_1} - \mathbf{r_2}$. If their interaction was predominantly of electrostatic nature, $\boldsymbol{\delta a}$ and $\boldsymbol{\delta r}$ were (anti)parallel.

We have performed the above-mentioned analysis on every 25th frame of the dataset that shows the smallest mean acceleration values and is thus most likely to show charge biases. Increasing the number of frames did not qualitatively change the results. Figure 4(a) shows histograms of the angle between $\boldsymbol{\delta a}$ and $\boldsymbol{\delta r}$. For large inter-particle distances, we observed a clear preference for a perpendicular alignment between $\boldsymbol{\delta a}$ and $\boldsymbol{\delta r}$ (as expected for fluid forces), whereas a parallel alignment (expected for electrostatic interactions) did not occur. At inter-particle distances of <180 μm, the probability distribution functions (PDFs) were shifted toward larger angles, indicating that the particles accelerate away from each other. This is corroborated by Fig. 4(b), where we calculated the mean magnitude of the particle acceleration projected onto their separation line $\mathbf{r}$. While this value is expected to increase toward smaller separations in turbulent flows with uncharged particles,[55] there is no reason for the repulsive interactions to be more pronounced than the attractive ones at those small and isotropic scales. We interpret the mismatch as the result of charges on the particles, which allows us to obtain a rough estimate of the electrostatic force between them. The inset in Fig. 4(b) shows this difference and a fit of C/r^2. By applying Coulomb's law, we obtain an estimate for the charge on each particle (~10^4 elementary charges) from C.

The presence of charge effects at close distances is also seen in the radial distribution function (RDF). Figure 12 shows that going from larger to smaller increments, the RDF begins to decrease around 60 μm, which indicates the presence of a unipolar charge.[56,58] Following Chun *et al.*,[58] we can estimate the charge on the particles from the position of the peak around 60 μm. We arrived at 10^4 elementary charges in good agreement with the estimate presented earlier. This might, however, be an overestimate of the electric charge since it has been shown[59–61] that large-scale motions might lead to straining that appears as a decay in the radial distribution function.

IV. ILLUMINATION

The illumination of the particles was provided by a frequency-doubled TruMicro 7240 Yb:YAG laser (TRUMPF Laser GmbH, Schramberg, Germany) with a wavelength of 515 nm and a maximum energy of 7.5 mJ per pulse. It released pulses of 300 ns duration

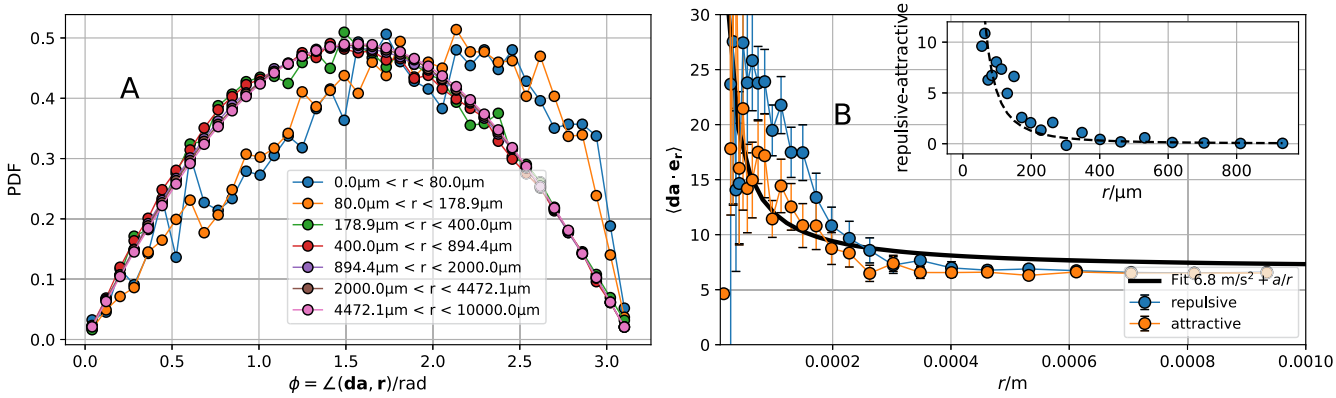

FIG. 4. (a) PDFs of the angle between the line of separation of two particles and the net acceleration (i.e., interaction force) between them. Parallel (antiparallel) alignment indicates an attractive (repulsive) interaction, whereas a perpendicular alignment is typical for an incompressible fluid. (b) Acceleration component along the line of separation of two particles. When the component is negative (positive), the interaction is seen as repulsive (attractive). The solid black line is a fit[55] ~$1/r$. *Inset:* Difference between parallel (attractive) and antiparallel (repulsive) acceleration components. Due to the isotropy of small scales <10η, we interpret this difference as a result of the effective electrostatic forces. The dashed line is a fit ~$1/r^2$ from which we estimate the charge on the particles.

at 20–100 kHz, yielding a maximum power of 300 W. The laser is commonly used for precision-welding applications but was also used in the research context to illuminate cloud droplets.[10] It featured a low-power alignment laser (Class 2, 630–680 nm), which made the alignment of optics in the open experimental hall and inside the tunnel safe. The high-power Yb:YAG laser was only operated when the tunnel manholes were closed and secured from operation otherwise through adequate procedures for laser safety.

The laser beam was guided through a 30 m long optical fiber (LLK-D06, 100 mm mrad, TRUMPF Laser GmbH) into a light-sealed box. The box enclosure contained a custom mount for the optical fiber connector on one side and a round hole on the opposite, tunnel-facing side. The bottom of the box consisted of an optical breadboard. The box was mounted flush on the optical access flange of the wind tunnel, and the remaining gaps were covered with laser safety fabric. Its support structures were fixed to the facility walls, such that the relative motion between the laser beam and the wind tunnel was minimized. The beam left the fiber at a divergence angle of (73 ± 4) mrad. We used a single collimating lens and a beam-expander to generate an almost parallel, ~4 cm wide beam. The remaining divergence angle was so small that no further beam-shaping optics were needed despite the ~12.5 m long beam path. This meant a substantial simplification of the optical setup since the focal length of optics within the wind tunnel depends on the facility pressure.

The beam entered the tunnel through a pressure sealed window (Typ 76, METAGLAS GmbH). The window was protected by a ball valve, which automatically closes in case the window would break and an outflow would ensue. In this case, the laser safety circuit was automatically triggered, preventing the laser from shining into the closed ball valve. The beam entered at an angle such that the fraction of light reflected from the uncoated, thick window was not focused back into the fiber.

Inside the tunnel, the beam was not enclosed further. The beam path within the facility is illustrated in Fig. 1. It first crossed the measurement section perpendicular to the flow direction toward a mirror. Its kinematic mount (AC-8823, Newport Optics) can be remotely adjusted by ±3.5° from outside the facility, which was the only means of adjusting the beam path once the wind tunnel was pressurized. The beam was directed onto a 2-in. mirror fixed onto the tunnel floor using conventional lens posts. A 3D-printed aerodynamic housing had been manufactured for this mirror to reduce the flow disturbance, prevent misalignment by the flow, and reduce the cover of particles.

The beam was then directed toward the imaging setup ~6.5 m downstream of the beam entry into the tunnel. Starting from the wind tunnel ceiling, an arrangement of fixed-angle mirrors guides the beam such that it forms an "X" parallel to the wind-tunnel cross section (see Figs. 1 and 5). The intersection of the "X" is a double-cone with a maximum diameter of 4.5 cm. In this region, where the laser beam passes twice, the amount of light is sufficient to illuminate the 10 μm large particles to allow tracking even when they are slightly out of focus. The configuration has the additional advantage that all cameras experience similar scattering angles, even though they observe the measurement volume from four opposite directions (see Sec. V). The particle image intensities resulting from this illumination are relatively homogeneous across the measurement volume.

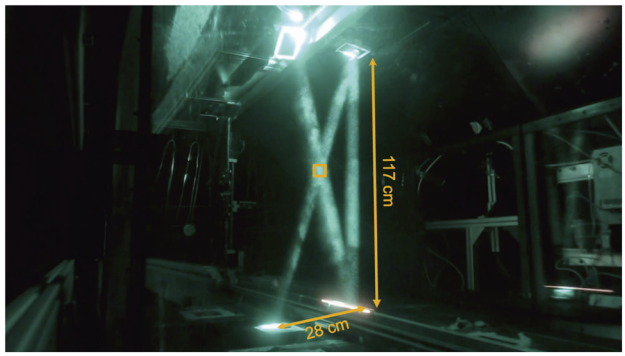

FIG. 5. Self-crossing laser beam forming the measurement volume at its intersection. The laser beam first hit the upper left mirror and was dumped onto the steel floor in the lower left corner of the "X." Brighter spots in the beam were due to "clouds" of particles passing by.

The beam was dumped onto a black steel floor panel. The position of the beam on the mirrors could be observed through several webcams. In addition, we used a flat plate on a remote-controlled traverse (the opposite side of the calibration mask) to observe the position of the alignment laser. We marked the correct beam position at well-defined traverse positions while the tunnel was open and accessible for maintenance. When it was filled with SF_6, it was then straightforward to check the beam position using a standard webcam. We observed that the beam position moved by up to a centimeter when changing the tunnel pressure. Please note that the tunnel could deform by up to 0.5 cm under pressure, which in turn moved the mirrors mounted to the walls. This likely explains the observation. The shifts in the beam position were corrected using the remote-controlled kinematic mirror.

A train of laser pulses of pre-defined frequency and duration was released upon receiving a digital signal from the digital signal generator described in Sec. V. This was realized through the proprietary programming interface of the laser device. The laser frequency was set to the camera sampling frequency or a multiple thereof, and the duration of the illumination was chosen as 4–10× the video duration (0.56 s).

V. IMAGING AND OPERATING PROCEDURES

Modern Lagrangian particle tracking relies on the ability of high-speed digital cameras to capture the positions of multiple particles sufficiently fast to allow their reliable frame-by-frame tracking in a vigorous turbulent flow. Full information can only be extracted in three-dimensional particle tracking, which requires at least two cameras. However, three cameras dramatically increase the fraction of trackable particles, and four cameras allow the noise-free reconstruction of acceleration statistics.[31,62]

The particle tracking setup presented here allowed for the simultaneous recording of up to four Phantom v2511 high-speed cameras. These cameras had a maximum recording speed of 25.6 Gpx/s (25 kHz at full resolution of 1280 × 800 px). They had been customized by the manufacturer to allow their operation under varying external pressure. Specifically, the protective glass on top

of the sensor was vented to allow for pressure equilibration. Otherwise, as observed with most electronic equipment, the cameras could be operated unaltered in pressurized SF_6. Immersing the cameras inside the gas-filled tunnel also avoided additional changes in the refractive index within the optical path of the imaging optics. The camera recording frequency was synchronized with the laser pulse frequency. Recordings were triggered by the digital output interface described below.

The camera optics consisted of an AF Micro-Nikkor 200 mm 1:4D IF-ED camera lens, whose aperture was set to $f/11$, and two 2× teleconverters, resulting in a magnification close to 1 when focused to the center of the measurement volume. Since the refractive index of SF_6 depends sensitively on the pressure,[50] the cameras need to be refocused after changing pressure. We mounted a timing belt to the manual focus rings of each 200 mm camera lens and connected them mechanically to stepper motors (Trinamic QSH2818-51). The motors were controlled remotely through an Arduino Motor Shield using a MATLAB program as an external interface.

The cameras and imaging optics were mounted on spring-suspended platforms as illustrated in Fig. 6. The springs connected the platforms to a sled, which rests on the tunnel rail system.[3] This arrangement effectively decoupled the imaging setup from the tunnel structure, which vibrated during operation. The remaining motions of the cameras and imaging optics were eliminated by the dynamic camera calibration of the particle tracking code.

To extract real-world physical measurements from the sensor coordinates, the cameras needed to be calibrated. That is, the sensor coordinates on each camera needed to be related to coordinates in the three-dimensional measurement volume. A standard method to perform such a camera calibration is the placement of a flat plate with known features (e.g., dots or a square pattern) at different positions within the measurement volume. Knowledge of the exact calibration plate position is not strictly necessary[63,64] if the angle of the calibration plate with respect to the sensor plane can be changed significantly. In the enclosed environment, it was easier to linearly traverse a calibration plate through the measurement volume and record the traverse positions. Since the cameras were refocused at each measurement pressure, their imaging model needed to be updated *in situ*, and the calibration had to be remotely controllable. We thus mounted the calibration plate on a 500 mm linear stage (igus GmbH), which was mounted on an existing horizontal instrumentation traverse. The calibration plate was a printed grid of 1 mm diameter black circles with 2 mm grid spacing glued onto a flat aluminum plate. Three of these circles were marked as fiducial markers. The calibration plate was illuminated by an LED strip.

A typical calibration procedure consisted of moving the horizontal traverse such that the calibration plate was visible on the high-speed cameras, traversing the plate through the measurement volume in steps of 2 mm (traverse reading), and returning the instrument traverse to its original position at the downstream end of the

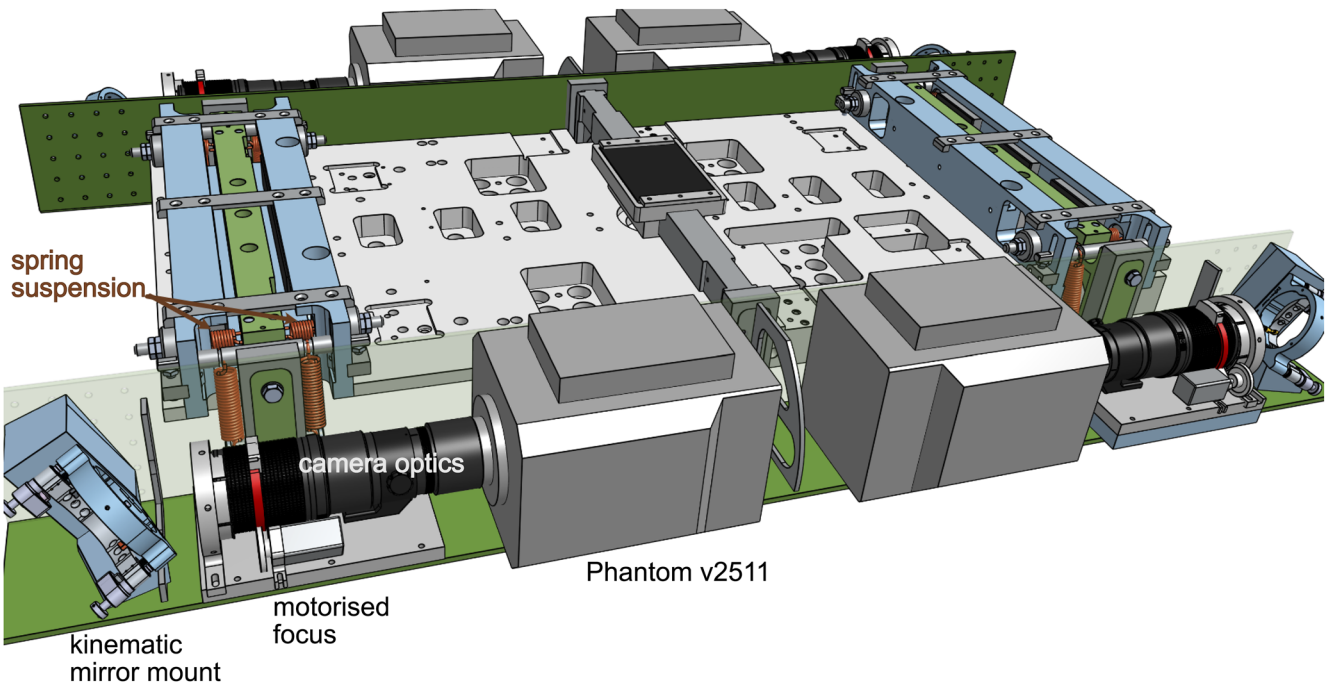

FIG. 6. Camera platform located underneath the wind tunnel floor. The two camera support structures (green) were connected rigidly with each other but connected to the rest of the platform through vibration/damping springs (red). Each of the four high-speed cameras observed the measurement volume through a 200 mm telephoto lens, two 2× teleconverters, a mirror, and an optical window. The mirrors could be remotely adjusted by motors. The lenses were focused remotely through timing belts, which were moved by a stepper motor. The measurement volume was located ~60 cm above the center of the traverse.

wind tunnel section. Small motions in the position of the traverse and imperfections in the traverse mechanics and position reading made this calibration relatively imprecise. It was therefore only used as a starting point, and the necessary precision was achieved by the on-track calibration and dynamic self-calibration of the tracking code (see Sec. VI and Bertens *et al.*[10]).

The camera clocks controlling the exposure of a single frame were linked together to the laser master clock. The video download and camera setup occurred over 1 or 10 GbE connections. The cameras were connected to network switches located inside the wind tunnel. A conventional Ethernet cable (1 GbE) and three pairs of optical fibers connect these switches to the outside of the facility through electrical and optical feedthroughs, respectively. The download rate over the 10 GbE connection varied between 2 and 8 Gb/s, such that the acquisition of a single experiment (96 GB in total) with four cameras took between 4 and 10 min.

The data acquisition was controlled by TTL-signals over coaxial cables. The magnetically actuated valves, the proprietary laser interface, and the camera triggers were connected to a National Instruments USB-6229 Digital I/O USB-interface. This interface was controlled by a custom MATLAB-program, which sent signals to the valves, laser, and cameras in a pre-defined sequence. Specifically, the magnetically actuated valve 1 was opened first to pressurize the particle dispenser. After 1.5 s, valve 2 was opened for a user-defined time to release a puff of particles. Valves 1 and 2 were then closed, and the program waited for a user-defined time to release laser pulses. After a third user-defined time, the program sent a trigger signal to the cameras, and they started their acquisition. This process could

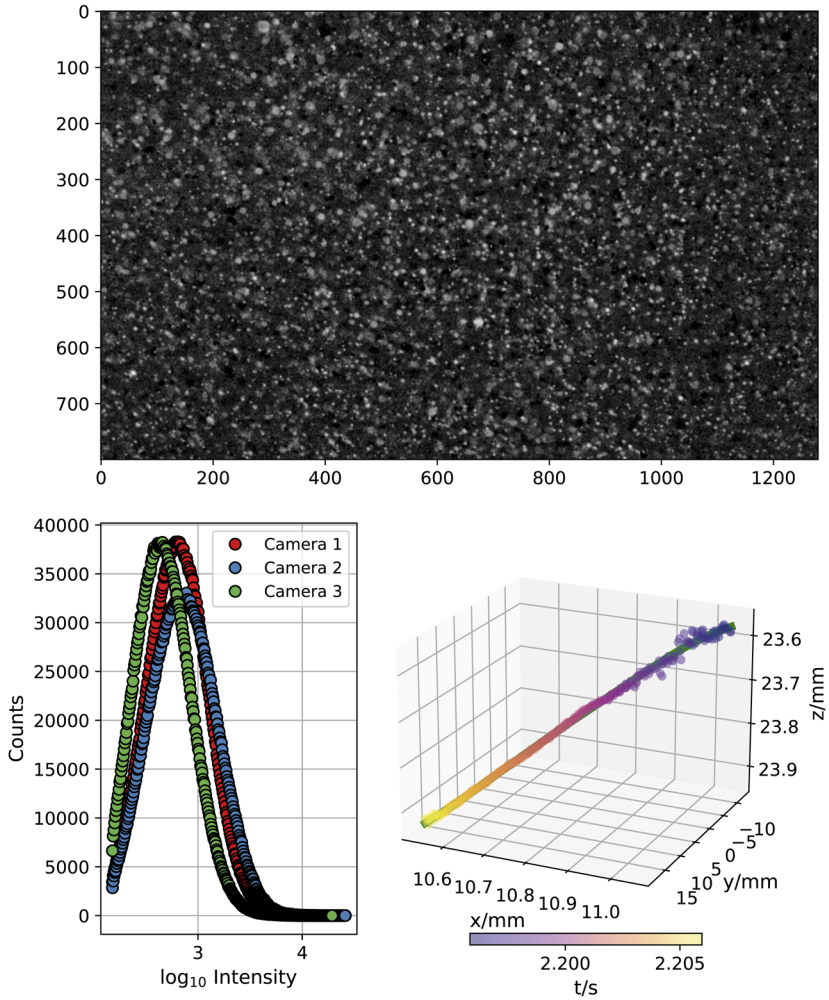

FIG. 7. Particle tracking properties. *Top:* Sample frame with a relatively large seeding density on Camera 2. Note the diffraction patterns of out-of-focus particles, which we used to inform particle triangulation about the sensor-particle distance. *Left:* Histograms of the logarithm of the particle intensity. *Right:* Single sample track with raw data color-coded in time and the resulting smoothed track in green.

be started automatically once the videos had been downloaded, i.e., several experiments could be carried out successively without supervision.

VI. TRACKING CODE

Figure 7 shows a sample frame from a typical video taken under the conditions specified in Table II. To track the cellulose particles, we used the particle tracking algorithm originally developed for *in situ* tracking of cloud droplets.[10] Many of the experimental challenges faced there, such as insufficient illumination or large sweeping flow, were present here to an even larger degree. In particular, the necessarily small size of the particles resulted in a very low amount of light scattered by them onto the camera sensors, even with relatively large aperture diameters used ($f/11$). Figure 7 shows an example of the intensity distribution on a typical video. This leads to a low signal-to-noise ratio and less position accuracy of the images. On the other hand, unlike the cloud droplet the cellulose particles were always small enough so that they could be considered as point sources of light, making our choice of point spread function universally valid.

The thermal gradients generated by the camera fans, combined with the high dependence of the index of refraction on temperature for SF6 at high pressure, significantly lower the image quality and shift the apparent centers of the particle images in a manner that cannot be accommodated by the camera model self-calibration. These apparent shifts precluded the usage of the standard shake-the-box algorithm and justified our changes to it as described below.

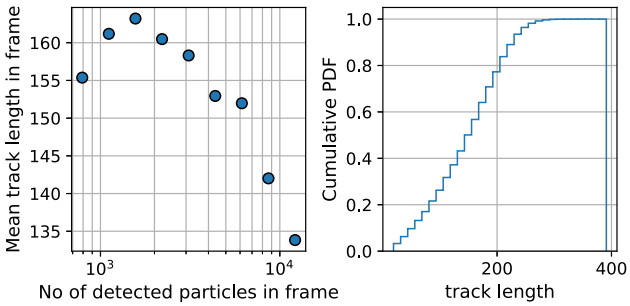

FIG. 8. Track characteristics. *Left:* Binned mean track lengths in frames vs the number of particles detected in the frame. In more densely seeded videos, the tracks were only slightly shorter on average. *Right:* Cumulative PDF of the track lengths. The majority of tracks were shorter than 200 frames (corresponding to about 4 τ_η for the present experiment). A particle crossing the measurement volume at mean flow velocity was visible for ~230 frames.

The detailed description of our particle tracking algorithm warrants a separate publication, and its main features have been described in Bertens *et al.*[10] Here, we briefly summarize the parts that are crucial to successful tracking in our wind tunnel.

The tracking algorithm is broadly based on the shake-the-box (STB) algorithm developed by Schanz *et al.*[42] for a pinhole camera model with lens distortion.

Like the standard STB, we used the progressive subtraction of already-tracked objects and iterative improvements of their fitted parameters. Unlike the standard STB, we did not tie the particle image locations to the particle three-dimensional positions (as the thermal gradients make the link unreliable), but only used the projected image positions as starting guesses for the iterative optimization process, which happened entirely in two dimensions. We also used a more sophisticated stereoscopic reconstruction process, which took into account not just image locations but also their brightness and defocus. To this end, we obtain a calibration between the line-of-sight coordinate of each camera and its level of defocus. The defocus was measured by fitting the point spread function to the individual images' radial intensity profile. For details, see Bertens *et al.*[10] Nevertheless, the low amount of light scattered from the small particles limits the positional accuracy of the raw tracks to 0.2–0.3 px (5.6–8.4 μm). The temporal linkage was delayed by several frames relative to the current frame (we chose to delay by six frames at 25 kHz), which was achieved by making each trajectory consist of potentially several heads (which temporally link the most recent positions) and a single tail. The tail was extended by choosing its most likely continuation from the backs of all heads, after which the heads not connecting to the extended tail were pruned. This delayed decision process allowed us to deal with the short residence time of the particles in our stationary setup and allowed reliable temporal linkage even in the presence of strong accelerations. For a more detailed description of the tracking algorithm, see Bertens *et al.*[10]

Figure 8 indicates that the tracking and postprocessing led to tracks that were slightly shorter than expected from the mean flow velocity (240 frames for the present experiment). The detected tracks were slightly less at larger seeding densities owing to the increased difficulty of assigning detected particles to existing tracks with confidence. Using 2000 particles per frame as a typical value for our tracking system, a comparison to earlier efforts was possible by comparing the number of particles that were tracked in a given volume. It can be seen in Table I that our experiment did not achieve the

TABLE I. Tracking the performance of selected experiments. While the positioning accuracy of all four experiments is between 0.1 and 0.4 pixels, the number density of particles has improved massively since the introduction of the shake-the-box algorithm Schanz *et al.*[42] All Reynolds numbers are Taylor-scale Reynolds numbers, except for the channel, where the friction Reynolds number is given (*).

	Channel[39]	LEM[31,35]	Jet[42]	VDTT
Re	250*	100–504	250	200–6000
Measurement volume (mm^3)	150 × 150 × 5	20 × 27 × 41	12 × 12 × 54	40 × 40 × 40
Particles/mm^3	0.003	0.05	0.9	0.06

massive particle densities in the optimized experiments by Schanz *et al.*[42] but obtained a similar number of densities as other experiments at lower R_λ. The shake-the-box principle that was applied for the Lagrangian Exploration Module, Jet, and in this work, allowed for much higher number densities than the principle of minimum acceleration employed in the channel flow experiment.[39] Interestingly, all four selected experiments had similar subpixel accuracies between 0.1 and 0.3 px, which appears to be difficult to improve. Of course, advances in camera technology have enabled substantial progress in absolute positional accuracy.

VII. POSTPROCESSING OF RAW TRACKS

The overall aim of the setup was to measure particle velocity and acceleration in the Lagrangian sense. To characterize the flow—in particular the rate of dissipation of turbulent kinetic energy—access to Eulerian quantities is desirable as well. The raw tracks contain random noise, systematic instrumentation-induced errors, and statistical sampling biases due to the time-dependence of the particle seeding. In the following, we describe the processing steps implemented to reduce these biases.

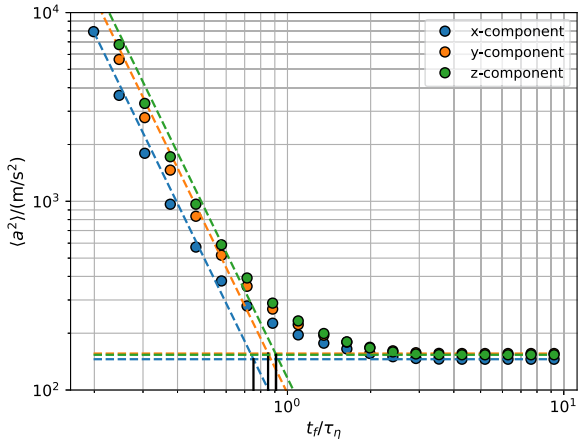

FIG. 9. Procedure to find the ideal smoothing length t_f normalized by τ_η. At small t_f, noise dominates the acceleration variance, yielding too high values. For large t_f, $\langle a^2 \rangle$ approaches a constant (horizontal dashed lines), indicating over-smoothing. Close to the transition to $\langle a^2 \rangle \approx$ const., $\langle a^2 \rangle \sim t_f^{-3}$ (falling dashed lines). We choose the intersection of these two lines as ideal filtering lengths (solid black lines).

A. Random noise

To remove random noise from the trajectories, three methods are commonly used in the literature: Smoothing by convolution with (differentiating) Gaussian kernels is a frequently used technique (e.g., Mordant *et al.*[62]) and is similar to a conventional window smoother. However, the filter operation is undefined at the edges, which leads to a loss of data and a selection bias in the resulting statistics.[31] The first Lagrangian measurements at high Reynolds numbers employed the Savitzky–Golay-filter (polynomial fits through portions of a track) to remove random noise from the raw trajectories.[17] However, the resulting statistics were very sensitive to the choice of the filter length (the length of portions), and the filter was undefined at the edges of a track, although the effect was smaller than in the Gaussian filter.[17] B-Spline filtering[65] was made popular for smoothing Lagrangian particle tracks in turbulent flows by Gesemann *et al.*[66] and compared to Gaussian filtering by Lawson *et al.*[31]

We implemented a version of the B-Spline algorithm after Eilers and Marx.[65] We used the tracking code's internal measure of triangulation quality, namely the ratio of individual and typical triangulation error (sum of square distances between the projection of best-fit particle position and particle image over all cameras), to construct a weighting matrix. This reduced the filtering time scale by more than 50%. To obtain an optimal filtering length t_f, we calculated the acceleration variance for a range of t_f and applied the following procedures illustrated in Fig. 9. For choices of t_f, where noise dominated the acceleration statistics and the smoothing is insufficient, $\langle a^2 \rangle \sim t^{-3}$. For large values for t_f, $\langle a^2 \rangle$ approached a constant. In this latter regime, the tracks were over-smoothed, and the reconstructed trajectories did not resemble the data appropriately. We, therefore, choose the intersection of the $\langle a^2 \rangle \sim t_f^{-3}$-line and the $\langle a^2 \rangle$ = const. as the "ideal" smoothing parameter. Figure 7 shows an example result of the smoothing procedure. On average, particle positions were shifted by about 5 μm during the smoothing procedure, indicating that the system has a spatial resolution below η.

The edges of the measurement volume are expected to be preferentially sampled by slow particles with little acceleration since fast particles have a higher probability to be advected out of the measurement volume. We mitigated this bias by calculating spatially resolved, time-averaged velocity statistics and identifying the boundary regions, where mean and RMS velocity differ from the center.

B. Inhomogeneous particle seeding

The amount of particles per frame is critical for the statistical and spatial resolution of Eulerian quantities. The active grid causes the turbulence intensity to vary strongly from eddy to eddy. Depending on the mean flow speed and active grid agitation, the particle tracking setup "sees" between 0.5 and 5 large eddies of size L per video. In previous measurements with nanoscale hot wires,[45,67] averaging over several hours was a straightforward strategy to achieve well-resolved statistics. While more videos can be taken, the statistical convergence obtained with single-point hot wire measurements remains out of reach. Moreover, the particle seeding throughout one video varied massively, such that some parts of the bypassing flow contributed disproportionately toward the ensemble statistics. Since even second-order flow statistics, such as the turbulence dissipation rate ε, have a heavy-tailed distribution, this can cause severe biases at all scales.

The combined unsteadiness of the flow and its seeding must be considered when calculating Eulerian quantities, e.g., to obtain the rate of dissipation. We refer to Sec. VIII for an example of a potential strategy to mitigate these biases.

TABLE II. Parameters of the sample measurement chosen to characterize the measurement.

R_λ	$\varepsilon/(\mathrm{m}^2/\mathrm{s}^3)$	P (bar)	U (m/s)	u_{RMS} (m/s)	τ_η (ms)	η (μm)	St
2700	0.1	6	4.16	0.42	2.0	28	0.16

VIII. CHARACTERIZATION

In the following, we analyze a representative measurement taken with the setup described here. The turbulence parameters can be found in Table II. Note that we used only three cameras when acquiring these data due to a single camera malfunctioning. We show in the following that we were nevertheless able to obtain useful data.

We begin by characterization of the flow within the measurement volume, which was intended to be homogeneous and isotropic. To test this, we calculated the mean, standard deviation, and Reynolds stresses for the three velocity components. To remove biases from fluctuating seeding densities, we first calculated the mean velocities binned along the x axis in each frame. We then proceeded to calculate the standard deviation, mean, and Reynolds stresses over time. The results for the x-direction, i.e., horizontally perpendicular to the flow, are shown in Fig. 10. The mean flow was subtracted from all components. No substantial mean shear could be found within the measurement volume, confirming earlier findings in Küchler.[47] The standard deviation of the velocity components transverse to the mean flow direction (u and w) were very close to each other, whereas the fluctuations in flow direction were about 1.2× larger. This suggests the presence of anisotropy at the largest scales, most likely caused by the temporal correlation of the active grid. To elucidate to what extent this large-scale anisotropy persisted at smaller scales, we compared the longitudinal and transverse Eulerian second order structure functions, S_2 and S_2^T, respectively (see below for details). The isotropic relation $S_2^T(r) = S_2(r) + (r/2)(\partial S_2(r)/\partial r)$ was in good agreement with our direct measurement of S_2^T, indicating that at the high R_λ, we investigated here, the small-scale anisotropy was small.

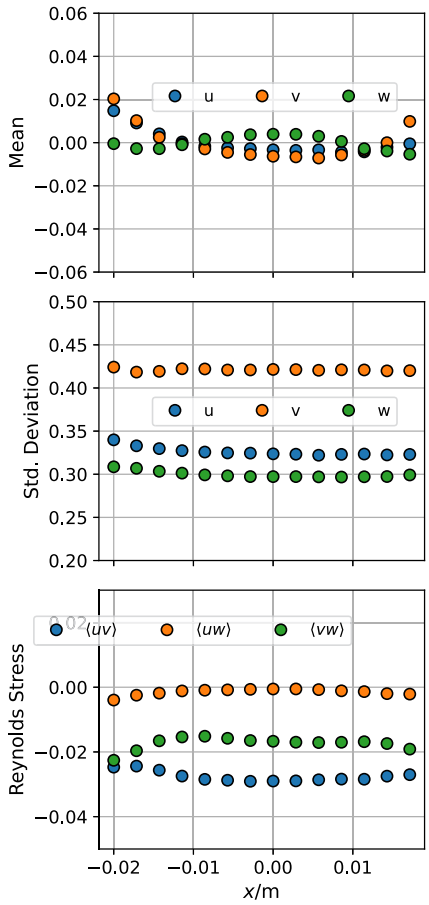

FIG. 10. Measures of large-scale homogeneity and isotropy. The particle velocity components and Reynolds stresses have been averaged within each frame and x-bin, and their overall mean has been removed. Then the mean and standard deviation have been calculated over all frames. No substantial shear was observed, and the velocity profiles showed only minor deviations toward the edges. The velocity fluctuations (i.e., standard deviation) were stronger in the streamwise direction than in the transverse direction.

A. Parameter ranges

To characterize the data acquired from the setup, we study the range of accessible parameters theoretically. Based on the range of mean flow speeds (0.5–5 m/s), energy injection scales (0.1–0.5 m), and a typical turbulence intensity of 10%, we used $\varepsilon = u_{RMS}^3/L$ to estimate the Reynolds number and Kolmogorov time scales τ_η accessible in the experiment. u_{RMS} denotes the RMS of the fluctuating velocity component. We further estimated the maximum track lengths that can be expected based on the length of the measurement volume in the mean flow direction (4 cm). Figure 11 shows that low integral length scales and high pressures are advantageous if long track lengths are required, whereas a high relative temporal resolution can be obtained at large values of L and lower pressures. The parameter space at the largest Reynolds numbers is naturally limited to the most extreme parameters possible in the facility. While the choice of mean flow velocity U appears to be unimportant at a given turbulence intensity, a subtle effect is not captured in this illustration: Thermal plumes rising from the warm high-speed cameras considerably impacted the video quality at larger pressures (> 6 bar) due to the strong temperature-dependence of the refractive index.[50,68] Higher mean flow speeds help improving the video quality since they advect these thermal plumes away from the cameras.

We emphasize that the facility was capable of generating one R_λ with a variety of parameter combinations. In particular, the effects of the particles' finite Stokes number could be investigated by performing multiple experiments at a single R_λ but different τ_η. Since larger cellulose particles were available from the manufacturer, this furthermore allows in principle the systematic study of inertial particle dynamics in turbulence over a wide range of Reynolds and Stokes numbers. Figure 3 shows that the Stokes number is below 0.1 (and the particles are, therefore, good tracers) for Reynolds numbers up to 3000. By changing the experimental parameters, particle dynamics up to St ≈ 1 can be measured at the same Reynolds number. This opens, for example, the possibility for studies on the effect

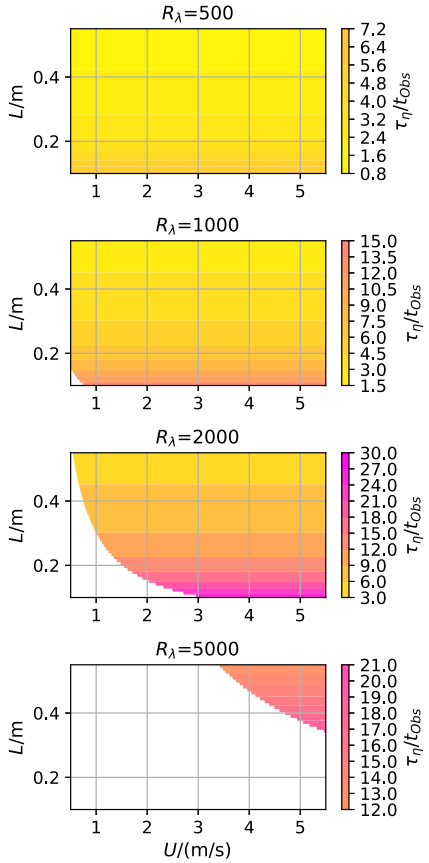

FIG. 11. Number of τ_η for which a particle remained observable at different R_λ given a turbulence intensity of $u_{RMS}/U = 0.1$, as a function of U and L. A given R_λ can be obtained in multiple ways by adjusting the viscosity through the facility pressure, L through the active grid, and U using the wind tunnel fan. Smaller L and smaller viscosity allowed a larger number of τ_η to be observed before the particles left the measurement volume. White areas indicate parameter combinations inaccessible to the facility.

of particle size on clustering dynamics at atmospheric Reynolds numbers, which is of great interest to studies of cloud formation.

B. Radial distribution function

An important question in the study of particles in a turbulent environment is how they distribute spatially within a flow. A perfect tracer will homogeneously seed the flow, but particles with finite inertia will be expelled from regions with strong vorticity, leading to an undersampling of those regions and a clustering of particles in other regions (e.g., Gibert *et al.*[69]). Such clustering effects are captured by the relative probability of finding a particle at a distance r away from a different particle, i.e., the radial distribution function (RDF). For perfect tracers, the RDF is independent of r, whereas clustering leads to an increase of the RDF at small r. A simple way of obtaining the RDF is to calculate the probability of finding a certain r within a dataset and compare it to the probability of finding a certain r in an artificial frame containing a random sample of particles from the dataset. This latter step accounts for the reduced detection frequency of points close to the boundary or other setup-specific biases. A detailed account of this procedure is given in Saw.[70] Figure 12(a) shows the RDF for a flow at $R_\lambda \approx 2700$ measured at a pressure of 6 bar. We can identify five regions in this plot going from large separations toward small: (I) the drop at large scales $>100\eta$, which can be attributed to residual large-scale inhomogeneities due to incomplete mixing,[71] (II) the approximately flat region indicating a uniform distribution of particles, (III) the initial clustering due to finite stokes numbers, (IV) the strong clustering at scales $<4\eta$, and the drop of the RDF at very small scales <60 μm, which is likely caused by charges on the particles as detailed in Sec. III. Region (III) can be approximated by a power law with an exponent of 0.2, which indicates a Stokes number of 0.2 in good agreement with the parametric estimate for this dataset. Region (IV) is reminiscent of a recent experimental result by Hammond and Meng,[72] where the RDF shows a strong increase going toward very small separations. This feature requires further in-depth investigation beyond the scope of this paper.

C. Eulerian structure functions

The statistics of spatial velocity increments are a ubiquitous quantity in the study of turbulence at small scales and, therefore, a prime quantity to assess the capability of the setup to measure velocity statistics. Here, we study the so-called longitudinal structure functions defined as $S_2 = \langle((\mathbf{u}(\mathbf{x}) - \mathbf{u}(\mathbf{x}+\mathbf{r}))\cdot\frac{\mathbf{r}}{|\mathbf{r}|})^2\rangle = \langle du(r)^2\rangle$, i.e., the variance of the velocity difference at two points separated by r projected onto r. It is accepted that to a reasonable approximation $S_2 \sim r^2$ at small increments, $S_2 \sim r^{2/3}$ in the inertial range, and $S_2 = u_{RMS}^2/2$ at large scales in the limit of large $r = |\mathbf{r}|$. In practice, we calculated $du(r)^2/du(r_{\max})^2$ for the particle pairs that we found within a frame, where $r_{\max}$ was the value in the largest increment bin and calculated the binned mean for each frame. The per-frame normalized structure functions were then averaged and rescaled by $\langle du(r_{\max})^2\rangle$. This procedure was inspired by Viggiano *et al.*[74] and accounts for the different large-scale statistics and seeding densities passing the measurement volume during a video. Figure 12(b) compares the longitudinal structure function obtained from particle tracks to the one measured by nanoscale hot wires at an earlier point using the same experimental parameters.[47] We see a very good agreement at scales >1 mm, but strong discrepancies at smaller scales and large statistical uncertainties. These may be caused by several effects. First, the number of frames containing data at small increments is relatively small (1–100), resulting in poor statistical convergence (see inset). Furthermore, at small increments with poor statistics, a precise measurement of the velocity increment is crucial, and an error of just 0.03 m/s in the velocity measurement leads to an error of 300% in the individual measurement of S_2. In hot wire measurements, these errors are mitigated by large statistics, and calibration errors cancel partially when calculating differences. Here, single velocity measurements with uncorrelated errors are subtracted, leading to large errors in the resulting structure functions. Furthermore, the data begin to diverge around 200 μm, where charge effects begin to play a role and might have an impact on the velocity difference statistics.

The transverse structure function S_2^T is obtained by considering those velocity components that are perpendicular to the line of separation between two particles. Under isotropic conditions, it is related

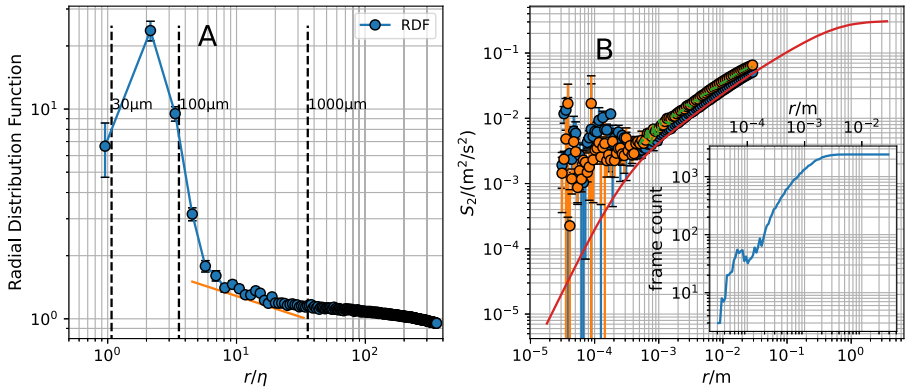

FIG. 12. Turbulence statistics from an experiment with $R_\lambda \approx 2700$ (see Table II for details). (a) Radial Distribution Function (RDF) of a representative experiment at $R_\lambda \approx 2700$ (see Table II) as a function of the inter-particle distance r normalized by the Kolmogorov length scale η. The orange line indicates the power law expected for St = 0.2 with an exponent of −0.2. The dotted lines indicate distances of 30 μm, 100 μm, and 1 mm. (b) Second-order longitudinal Eulerian structure function $S_2 = \langle(((\mathbf{u}(\mathbf{x}) - \mathbf{u}(\mathbf{x}+\mathbf{r}))\cdot\frac{\mathbf{r}}{|\mathbf{r}|})^2\rangle$ measured from particle tracks (blue circles) and nanoscale hot wires (red line).[47] Orange circles mark the second-order transverse structure function $S_2^T = \langle(((\mathbf{u}(\mathbf{x}) - \mathbf{u}(\mathbf{x}+\mathbf{r}))\cdot\frac{\mathbf{r}_\perp}{|\mathbf{r}|})^2\rangle$, where $r_\perp$ is a vector perpendicular to the line of separation. Green dashed lines mark the isotropic prediction of $S_2^\perp$ from S_2 (see text for details). *Inset:* Number of entries per bin.

to S_2 through $S_2^T = S_2 + (r/2)(\partial S_2/\partial r)$. This relation is shown as green dashed lines in Fig. 12. The agreement between the measured S_2^T and the one derived from S_2 indicates a small anisotropy in the inertial range.

D. Lagrangian statistics

In Fig. 13, we show Lagrangian statistics from the example measurements. The single-particle dispersion statistics were characterized by the mean squared displacement of the particles along the tracks averaged over all tracks. At small time increments, $\langle\Delta x^2\rangle \sim t^2$. At larger time increments $t > T_L$, should scale $\langle\Delta x^2\rangle \sim t$. However, even though weak flattening can be identified at the large t in our data, we do not reach the regime of $t > T_L$. The effect we observed is most likely an artifact due to the finite measurement volume: Faster particles tend to cross the measurement volume faster than slower ones, which resulted in a preferential sampling of slow particles at long times. This effect is well-known and even more important when considering the Lagrangian structure function in Fig. 13(b), which is defined here as $S_{2L} = \langle(u(t_0+t) - u(t_0))^2\rangle$ (averaging over all tracks and t_0). Berg *et al.*[75] suggest a scheme to compensate for this bias, which we have applied here. Comparing our data to the one from Xu *et al.*,[34] we see that we almost reach the Lagrangian inertial range, where we expect $S_{2L} \sim \varepsilon t$. Due to the aforementioned bias,

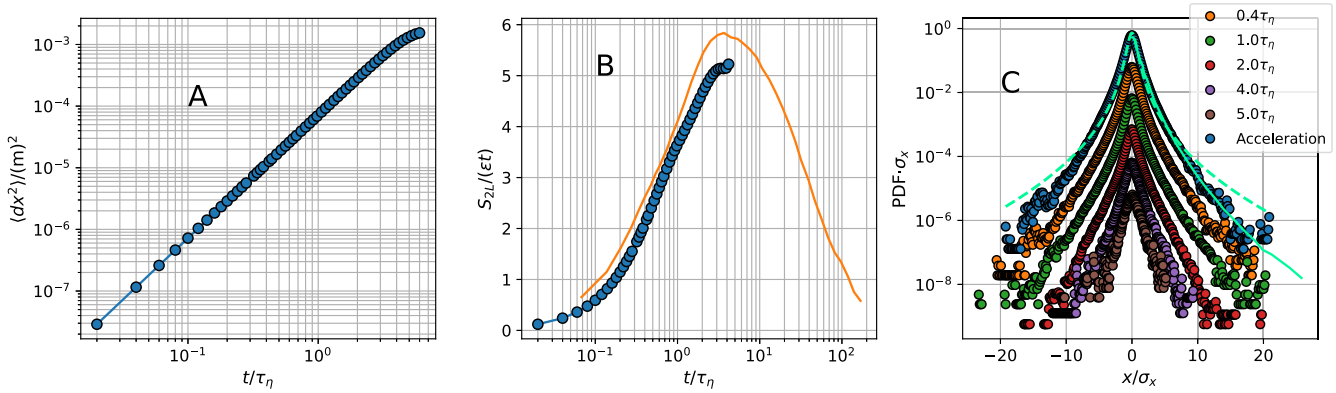

FIG. 13. Example Lagrangian measurements. (a) Mean squared displacement statistics of single particles. (b) Lagrangian velocity structure function of the *u*-component (blue) and data from Xu *et al.*[34] The size of the measurement volume and the mean flow velocity limited the track lengths to values just below the expected inertial range. Note that different choices of experimental parameters increased the observable range of τ_η. (c) PDFs of the velocity increments along the particle tracks and particle acceleration normalized by their respective standard deviations. Curves have been shifted by one decade for better visibility. The green dotted line is the stretched exponential typically found in the acceleration PDFs of tracer particles (Voth *et al.*,[17] Mordant *et al.*[62]). The green solid line is the PDF from DNS (Bec *et al.*[73]) at St = 0.16, which is close to the Stokes number found here.

it is not clear whether the data at the largest increments we could measure are the beginning of the inertial range or an incomplete compensation for finite measurement volumes.

The acceleration of (tracer) particles in a turbulent flow is of great fundamental importance since it is closely related to strong dissipative processes.[15–17,28,37] It is known to be a highly intermittent quantity with heavy-tailed PDFs.[28,62] We show measurements of the accelerations and the velocity increments along the particle trajectories in Fig. 13(c), i.e., $\Delta u(\tau) = \langle u_i(t_{j+\tau} - t_j)\rangle_{i,j}$, where $\langle\rangle_{i,j}$ denotes averaging over tracks and increments along tracks, respectively. The prominent strong tails can be seen in all increments studied and get progressively weaker with increasing separation as expected. For acceleration, Voth *et al.*[17] suggested a stretched exponential that has been shown to accurately describe acceleration statistics over a wide range of experiments and numerical simulations.[28,62] In Fig. 13(c), we show the stretched exponential in green with parameters obtained by Mordant *et al.*,[62] which lie above the data in the tails. The data are, however, in good agreement with data from numerical simulations[73] with a Stokes number of 0.16. This Stokes number is consistent with St calculated from the parameters of this experiment as well as the power law exponent found in the RDF. The PDFs of finite velocity increments show thinner tails as we increased the increment up to $5\tau_\eta$, which is the largest increment where such PDFs can be drawn sensibly given the length of the particle tracks.[31]

IX. DISCUSSION

We demonstrated an experimental setup capable of tracking particles in a turbulent flow at unprecedented R_λ. This widens the parameter space for Lagrangian measurements by about a factor of five compared to the previous state of the art. Lagrangian measurements have proven to be notoriously challenging and have only been available for little more than 20 years. This explains the large leap in Reynolds number that was possible using a single experiment. Our experiments are well above the Reynolds number that can be achieved in the largest direct numerical simulations of turbulence.[15] We have demonstrated that measurements of particle position, Eulerian and Lagrangian velocity increment statistics, and Lagrangian accelerations are possible. We have introduced cellulose particles as a seeding material for flow measurements, where small spatial (~10 μm) and temporal scales (~ms) have to be resolved. Our tracers are bio-compatible and allow humans to come into extensive contact with the material. The material might thus be considered as an alternative to visualize flows beyond the laboratory environment, e.g., for studies of thermal comfort or airborne disease transmission.[76–78] The illumination intensity currently limits the particle size to ≥10 μm, but smaller particles are available. To characterize the behavior of these particles as seeding material, we have measured their density and found their density to be about half that of solid cellulose, indicating the presence of voids in the material. Despite the decreased density, the particles cannot be seen as ideal tracers for a wide range of experimental parameters [see Fig. 3(d)]. However, the three independently adjustable flow parameters (mean velocity, grid setting, and pressure) allow the effects of the finite Stokes number to be systematically investigated while keeping the flow Reynolds number constant. At very large $R_\lambda > 3000$ 10 μm, Cellulobeads are inertial for all parameter choices.

These new particles further required the development of a dedicated particle dispenser. We validated that the dispenser released predominantly particle singlets. We further measured the charge on the particles as they appear in the measurement volume in two independent ways, yielding consistent values of about 10^4 elementary charges. The electrostatic forces appear in the radial distribution function, where very small inter-particle distances appeared to be depleted. However, <0.5% of particles came closer than 200 μm to another particle, such that electrostatic forces only needed to be taken into account when such small distances were explicitly of interest. The particle dispensers's reliability is an area of potential future improvement. For example, the number of particles released varies considerably between injections. While no measurement campaign had to be interrupted so far because of a failed particle release, the dispenser needed to be flushed regularly with a strong stream of SF_6 to loosen stuck material.

A serious challenge for the setup is the presence of thermal plumes, which can drastically distort the image at low flow velocities and high pressures. Their mitigation should be a priority in a next round of improvements of the setup.

Currently, the track length of the particles is limited to about 10 ms, due to the rapid advection of particles out of the relatively small measurement volume by the mean flow. This limits the setup to the measurement of velocity increment statistics up to ~$10\tau_\eta$, which makes a proper study of the Lagrangian inertial range very difficult.

In the example measurement shown here, we could track no more than $4\tau_\eta$. This is in reasonable agreement with the parameter study shown in Fig. 11, where a maximum track length of ~$6\tau_\eta$ was predicted for the given set of parameters. This means that with an optimized parameter choice, longer tracks (in terms of τ_η) could be obtained using the current setup. However, the parameters were chosen here to best resemble existing hot wire measurements for cross-validation of the results. The measurement volume also limits the range of scales, where Eulerian statistics can be computed to no more than 4000η. Enlarging the measurement volume would thus be another fruitful improvement of the setup, albeit a rather complex one.

In its current form, the setup can be used to measure acceleration and particle clustering statistics over a wide range of Reynolds- and Stokes numbers. Lagrangian velocity increment statistics can be obtained as long as only short increments are of relevance. While the focus of this work was on Lagrangian turbulence, the setup allows measurements of Eulerian quantities previously inaccessible within the facility. This includes transverse structure functions for increments $\gtrsim$ 1 mm and transverse components of single-point statistics, both of which are important to fully characterize the anisotropy in the flow. At large particle seeding densities, methods like Vortex-in-cell[79] or physics-informed neural networks[80] might be able to estimate the entire three-dimensional velocity field from the scattered data.

The setup is sufficiently general for most of its current limitations to be lifted in the future. For example, a different illumination source with longer pulse widths might make smaller and more tracer-like particles feasible since currently only 1% of the camera's exposure time is illuminated by the laser. An additional cooling system for the cameras would reduce the distortions due to thermal plumes. Finally, the camera setup is already connected to rails on

ball bearings and is, therefore, prepared to be moved along the flow, allowing tracking for much longer times. However, the flow properties and the maximum video length limit the current observation range to about 2 m. Still, this would, for example, allow for measurements of two-particle dispersion at high R_λ, which is of great fundamental and practical interest.

ACKNOWLEDGMENTS

The Variable Density Turbulence Tunnel is operated and maintained by A. Kubitzek, A. Kopp, M. Meyer, and A. Renner. We acknowledge A. Renner for continuous technical support throughout the project. We acknowledge G. Bertens, D. Fliegner, and H. Degering for help with networking and high-performance computing. The machine shop led by U. Schminke manufactured the camera platform and the particle disperser. We acknowledge F. Nordsiek for helpful discussions regarding particle choices and their interaction when charged. We acknowledge G. Bertens for providing optics and networking expertise as well as helpful discussions. We acknowledge B. Hejazi for help with data acquisition. We acknowledge H. Xu, A. Pumir, N. Ouellette, and G. Voth for their helpful discussions.

AUTHOR DECLARATIONS

Conflict of Interest

The authors have no conflicts to disclose.

Author Contributions

Christian Küchler: Conceptualization (equal); Data curation (equal); Formal analysis (equal); Investigation (equal); Project administration (equal); Software (equal); Supervision (equal); Visualization (equal); Writing – original draft (equal); Writing – review & editing (equal). **Antonio Ibanez Landeta**: Conceptualization (supporting); Data curation (supporting); Formal analysis (supporting); Investigation (supporting); Software (supporting); Writing – review & editing (supporting). **Jan Molacek**: Conceptualization (supporting); Methodology (supporting); Software (supporting); Writing – original draft (supporting); Writing – review & editing (supporting). **Eberhard Bodenschatz**: Conceptualization (equal); Funding acquisition (equal); Investigation (equal); Methodology (equal); Project administration (equal); Resources (equal); Supervision (equal); Writing – original draft (equal); Writing – review & editing (equal).

DATA AVAILABILITY

The data that support the findings of this study are available from the corresponding author upon reasonable request.

APPENDIX: CALCULATION OF PARTICLE CHARGES FROM THE RDF

According to Lu *et al.*,[56] particle charge causes a drop in the radial distribution function toward smaller distances r, i.e., the RDF peaks at $r = r_*$, where Coulomb- and inertial forces have similar magnitudes. They infer that

$$r_*^3 = \frac{2kq^2\tau_\eta\tau_p}{m_p B_{nl} c_1}, \tag{A1}$$

where m_p is the mass of the particle, q is its charge, and $k = 1/4\pi\epsilon_0$ is the Coulomb constant. B_{nl} (taken as 0.09 following Chun *et al.*[58]) is a dimensionless coefficient describing the particle pair diffusion, and $c_1 = 0.2$ is the exponent of the RDF power law, e.g., as an orange line in Fig. 12(a). Rearranging for q and reading off $r_* \approx 60\ \mu$m, we arrive at $\approx 10^4$ elementary charges.

REFERENCES

[1]A. S. Monin and A. Yaglom, in *Statistical Fluid Mechanics: Mechanics of Turbulence*, edited by J. L. Lumley (MIT Press, Cambridge, MA, 1975), Vol. 22.
[2]G. Comte-Bellot and S. Corrsin, "The use of a contraction to improve the isotropy of grid-generated turbulence," J. Fluid Mech. **25**, 657–682 (1966).
[3]E. Bodenschatz, G. P. Bewley, H. Nobach, M. Sinhuber, and H. Xu, "Variable density turbulence tunnel facility," Rev. Sci. Instrum. **85**, 093908 (2014).
[4]B. Rousset, P. Bonnay, P. Diribarne, A. Girard, J. M. Poncet, E. Herbert, J. Salort, C. Baudet, B. Castaing, L. Chevillard, F. Daviaud, B. Dubrulle, Y. Gagne, M. Gibert, B. Hébral, T. Lehner, P.-E. Roche, B. Saint-Michel, and M. Bon Mardion, "Superfluid high REynolds von Kármán experiment," Rev. Sci. Instrum. **85**, 103908 (2014).
[5]B. Saint-Michel, E. Herbert, J. Salort, C. Baudet, M. Bon Mardion, P. Bonnay, M. Bourgoin, B. Castaing, L. Chevillard, F. Daviaud, P. Diribarne, B. Dubrulle, Y. Gagne, M. Gibert, A. Girard, B. Hébral, T. Lehner, B. Rousset, and SHREK Collaboration, "Probing quantum and classical turbulence analogy in von Kármán liquid helium, nitrogen, and water experiments," Phys. Fluids **26**, 125109 (2014).
[6]J. Salort, C. Baudet, B. Castaing, B. Chabaud, F. Daviaud, T. Didelot, P. Diribarne, B. Dubrulle, Y. Gagne, F. Gauthier, A. Girard, B. Hébral, B. Rousset, P. Thibault, and P.-E. Roche, "Turbulent velocity spectra in superfluid flows," Phys. Fluids **22**, 125102 (2010).
[7]H. Kahalerras, Y. Malécot, Y. Gagne, and B. Castaing, "Intermittency and Reynolds number," Phys. Fluids **10**, 910–921 (1998).
[8]Y. Tsuji, "Intermittency effect on energy spectrum in high-Reynolds number turbulence," Phys. Fluids **16**, L43–L46 (2004).
[9]G. A. Rosi, M. Sherry, M. Kinzel, and D. E. Rival, "Characterizing the lower log region of the atmospheric surface layer via large-scale particle tracking velocimetry," Exp. Fluids **55**, 1736 (2014).
[10]G. Bertens, G. Bagheri, H. Xu, E. Bodenschatz, and J. Moláček, "In situ cloud particle tracking experiment," Rev. Sci. Instrum. **92**, 125105 (2021).
[11]N. Mordant, E. Lévêque, and J.-F. Pinton, "Experimental and numerical study of the Lagrangian dynamics of high Reynolds turbulence," New J. Phys. **6**, 116 (2004).
[12]N. T. Ouellette, H. Xu, M. Bourgoin, and E. Bodenschatz, "An experimental study of turbulent relative dispersion models," New J. Phys. **8**, 109 (2006).
[13]E. W. Saw, R. A. Shaw, S. Ayyalasomayajula, P. Y. Chuang, and Ã. Gylfason, "Inertial clustering of particles in high-Reynolds-number turbulence," Phys. Rev. Lett. **100**, 214501 (2008).
[14]F. Toschi and E. Bodenschatz, "Lagrangian properties of particles in turbulence," Annu. Rev. Fluid Mech. **41**, 375–404 (2009).
[15]D. Buaria and K. R. Sreenivasan, "Scaling of acceleration statistics in high Reynolds number turbulence," Phys. Rev. Lett. **128**, 234502 (2022).
[16]G. A. Voth, K. Satyanarayan, and E. Bodenschatz, "Lagrangian acceleration measurements at large Reynolds numbers," Phys. Fluids **10**, 2268–2280 (1998).

[17]G. A. Voth, A. La Porta, A. M. Crawford, J. Alexander, and E. Bodenschatz, "Measurement of particle accelerations in fully developed turbulence," J. Fluid Mech. **469**, 121–160 (2002).
[18]*Springer Handbook of Experimental Fluid Mechanics*, edited by C. Tropea, A. L. Yarin, and J. F. Foss (Springer, Berlin, 2007).
[19]Z. Rong, F. Chen, and H. Liu, "Scattering, tracking and seeding characteristics of TiO_2 using particle image velocimetry in supersonic flows," Mater. Test. **56**, 490–497 (2014).
[20]H. Wu, H. Xu, and E. Bodenschatz, "Measuring vorticity vector from the spinning of micro-sized mirror-encapsulated spherical particles in the flow," Rev. Sci. Instrum. **90**, 115111 (2019).
[21]B. Hejazi, M. Krellenstein, and G. A. Voth, "Using deformable particles for single-particle measurements of velocity gradient tensors," Exp. Fluids **60**, 153 (2019).
[22]N. A. Buchmann, C. Willert, and J. Soria, "Pulsed, high-power LED volume illumination for tomographic particle image velocimetry," Exp. Fluids **53**, 1545 (2012).
[23]O. Chételat and K. C. Kim, "Miniature particle image velocimetry system with LED in-line illumination," Meas. Sci. Technol. **13**, 1006–1013 (2002).
[24]T. Guimarães and K. T. Lowe, "Application of fluorescent particles for particle tracking velocimetry in wind tunnels," in *18th International Symposium on the Application of Laser and Imaging Techniques to Fluid Mechanics* (Lisbon Symposia, Lisbon, Portugal, 2016), p. 12.
[25]L. Kemp, E. C. Jamieson, and S. J. Gaskin, "Phosphorescent tracer particles for Lagrangian flow measurement and particle tracking velocimetry," Exp. Fluids **48**, 927–931 (2010).
[26]N. T. Ouellette, H. Xu, and E. Bodenschatz, "A quantitative study of three-dimensional Lagrangian particle tracking algorithms," Exp. Fluids **40**, 301–313 (2006).
[27]H. Nobach, N. Damaschke, and C. Tropea, "High-precision sub-pixel interpolation in particle image velocimetry image processing," Exp. Fluids **39**, 299–304 (2005).
[28]A. La Porta, G. A. Voth, A. M. Crawford, J. Alexander, and E. Bodenschatz, "Fluid particle accelerations in fully developed turbulence," Nature **409**, 1017–1019 (2001).
[29]*Three-Dimensional Velocity and Vorticity Measuring and Image Analysis Techniques: Lecture Notes from the Short Course Held in Zürich, Switzerland, 3–6 September 1996*, *ERCOFTAC Series*, edited by T. Dracos, P. Hutchinson, and W. Rodi (Springer Netherlands, Dordrecht, 1996), Vol. 4.
[30]H. Xu, "Tracking Lagrangian trajectories in position–velocity space," Meas. Sci. Technol. **19** 075105 (2008).
[31]J. M. Lawson, E. Bodenschatz, C. C. Lalescu, and M. Wilczek, "Bias in particle tracking acceleration measurement," Exp. Fluids **59**, 172 (2018).
[32]A. Schröder and D. Schanz, "3D Lagrangian particle tracking in fluid mechanics," Annu. Rev. Fluid Mech. **55**, 511–540 (2023).
[33]J. Lu, J. P. Fugal, H. Nordsiek, E. W. Saw, R. A Shaw, and W. Yang, "Lagrangian particle tracking in three dimensions via single-camera in-line digital holography," New J. Phys. **10**, 125013 (2008).
[34]H. Xu, M. Bourgoin, N. T. Ouellette, E. Bodenschatz, and International Collaboration for Turbulence Research, "High order Lagrangian velocity statistics in turbulence," Phys. Rev. Lett. **96**, 024503 (2006).
[35]R. Zimmermann, H. Xu, Y. Gasteuil, M. Bourgoin, R. Volk, J.-F. Pinton, E. Bodenschatz, and International Collaboration for Turbulence Research, "The Lagrangian exploration module: An apparatus for the study of statistically homogeneous and isotropic turbulence," Rev. Sci. Instrum. **81**, 055112 (2010).
[36]G. P. Bewley, K. Chang, E. Bodenschatz, and International Collaboration for Turbulence Research, "On integral length scales in anisotropic turbulence," Phys. Fluids **24**, 061702 (2012).
[37]S. Ayyalasomayajula, A. Gylfason, L. R. Collins, E. Bodenschatz, and Z. Warhaft, "Lagrangian measurements of inertial particle accelerations in grid generated wind tunnel turbulence," Phys. Rev. Lett. **97**, 144507 (2006).
[38]N. Stelzenmuller, J. I. Polanco, L. Vignal, I. Vinkovic, and N. Mordant, "Lagrangian acceleration statistics in a turbulent channel flow," Phys. Rev. Fluids **2**, 054602 (2017).
[39]N. A. Malik, T. Dracos, and D. A. Papantoniou, "Particle tracking velocimetry in three-dimensional flows," Exp. Fluids **15**, 279–294 (1993).
[40]H. G. Maas, A. Gruen, and D. Papantoniou, "Particle tracking velocimetry in three-dimensional flows: Part 1. Photogrammetric determination of particle coordinates," Exp. Fluids **15**, 133–146 (1993).
[41]R. Tsai, "A versatile camera calibration technique for high-accuracy 3D machine vision metrology using off-the-shelf TV cameras and lenses," IEEE J. Rob. Autom. **3**, 323–344 (1987).
[42]D. Schanz, S. Gesemann, and A. Schröder, "Shake-the-box: Lagrangian particle tracking at high particle image densities," Exp. Fluids **57**, 70 (2016).
[43]S. Tan, A. Salibindla, A. U. M. Masuk, and R. Ni, "Introducing OpenLPT: New method of removing ghost particles and high-concentration particle shadow tracking," Exp. Fluids **61**, 47 (2020).
[44]K. P. Griffin, N. J. Wei, E. Bodenschatz, and G. P. Bewley, "Control of long-range correlations in turbulence," Exp. Fluids **60**, 55 (2019); arXiv:1809.05126.
[45]C. Küchler, G. P. Bewley, and E. Bodenschatz, "Experimental study of the bottleneck in fully developed turbulence," J. Stat. Phys. **175**, 617–639 (2019); arXiv:1812.01370.
[46]M. Sinhuber, E. Bodenschatz, and G. P. Bewley, "Decay of turbulence at high Reynolds numbers," Phys. Rev. Lett. **114**, 034501 (2015).
[47]C. Küchler, "Measurements of turbulence at high Reynolds numbers—From Eulerian statistics towards Lagrangian particle tracking," Ph.D. thesis, Georg August University Göttingen, Göttingen, Germany, 2020.
[48]N. Hutchins, J. P. Monty, M. Hultmark, and A. J. Smits, "A direct measure of the frequency response of hot-wire anemometers: Temporal resolution issues in wall-bounded turbulence," Exp. Fluids **56**, 18 (2015).
[49]C. Küchler, E. Bodenschatz, and G. P. Bewley, "Universal Velocity Statistics in Decaying Turbulence," Phys. Rev. Lett. **131** (2023).
[50]M. E. Thomas and T. J. Tayag, "Refractive index of He, SF_6, and CO_2 at 063299 μm as a function of temperature and pressure," Appl. Opt. **27**, 3317 (1988).
[51]G. Z. Xiao, A. Adnet, Z. Zhang, F. G. Sun, and C. P. Grover, "Monitoring changes in the refractive index of gases by means of a fiber optic Fabry-Perot interferometer sensor," Sens. Actuators, A **118**, 177–182 (2005).
[52]J. Hoogland, H. Van Den Berg, and N. Trappeniers, "Measurements of the viscosity of sulfur hexaflouride up to 100 bar by a capillary-flow viscometer," Physica A **134**, 169–192 (1985).
[53]P. F. DeCarlo, J. G. Slowik, D. R. Worsnop, P. Davidovits, and J. L. Jimenez, "Particle morphology and density characterization by combined mobility and aerodynamic diameter measurements. Part 1: Theory," Aerosol Sci. Technol. **38**, 1185–1205 (2004).
[54]See https://pubchem.ncbi.nlm.nih.gov/compound/Cellulose for the density of cellulose; accessed 5 October 2022.
[55]M. Borgas and P. Yeung, "Conditional fluid-particle accelerations in turbulence," Theor. Comput. Fluid Dyn. **11**, 69–93 (1998).
[56]J. Lu, H. Nordsiek, E. W. Saw, and R. A. Shaw, "Clustering of charged inertial particles in turbulence," Phys. Rev. Lett. **104**, 184505 (2010).
[57]J. Lu and R. A. Shaw, "Charged particle dynamics in turbulence: Theory and direct numerical simulations," Phys. Fluids **27**, 065111 (2015).
[58]J. Chun, D. L. Koch, S. L. Rani, A. Ahluwalia, and L. R. Collins, "Clustering of aerosol particles in isotropic turbulence," J. Fluid Mech. **536**, 219–251 (2005).
[59]N. A. Malik, "Turbulent particle pair diffusion: Numerical simulations," PLoS One **14**, e0216207 (2019).
[60]N. A. Malik, "Turbulent particle pair diffusion: A theory based on local and non-local diffusional processes," PLoS One **13**, e0202940 (2018).
[61]N. A. Malik and F. Hussain, "New scaling laws predicting turbulent particle pair diffusion, overcoming the limitations of the prevalent Richardson–Obukhov theory," Phys. Fluids **33**, 035135 (2021).
[62]N. Mordant, A. Crawford, and E. Bodenschatz, "Experimental Lagrangian acceleration probability density function measurement," Physica D **193**, 245–251 (2004).

[63]K. Muller, C. K. Hemelrijk, J. Westerweel, and D. S. W. Tam, "Calibration of multiple cameras for large-scale experiments using a freely moving calibration target," Exp. Fluids **61**, 7 (2020).
[64]Z. Zhang, "A flexible new technique for camera calibration," IEEE Trans. Pattern Anal. Mach. Intell. **22**, 1330–1334 (2000).
[65]P. H. C. Eilers and B. D. Marx, "Flexible smoothing with *B*-splines and penalties," Stat. Sci. **11**, 89–121 (1996).
[66]S. Gesemann, F. Huhn, D. Schanz, and A. Schröder, "From noisy particle tracks to velocity, acceleration and pressure fields using B-splines and penalties," 18th International Symposium on the Application of Laser and Imaging Techniques to Fluid Mechanics (2016).
[67]M. Vallikivi, M. Hultmark, S. C. C. Bailey, and A. J. Smits, "Turbulence measurements in pipe flow using a nano-scale thermal anemometry probe," Exp. Fluids **51**, 1521–1527 (2011).
[68]J. M. St-Arnaud and T. K. Bose, "Direct determination of the intermolecular interaction contribution to the refractive index of carbon dioxide and sulfur hexafluoride," J. Chem. Phys. **71**, 4951–4955 (1979).
[69]M. Gibert, H. Xu, and E. Bodenschatz, "Where do small, weakly inertial particles go in a turbulent flow?," J. Fluid Mech. **698**, 160–167 (2012).
[70]E. W. Saw, "Studies of spatial clustering of inertial particles in turbulence," Ph.D. thesis, Michigan Technological University, 2008.
[71]E.-W. Saw, R. A. Shaw, J. P. L. C. Salazar, and L. R. Collins, "Spatial clustering of polydisperse inertial particles in turbulence: II. Comparing simulation with experiment," New J. Phys. **14**, 105031 (2012).
[72]A. Hammond and H. Meng, "Particle radial distribution function and relative velocity measurement in turbulence at small particle-pair separations," J. Fluid Mech. **921**, A16 (2021).
[73]J. Bec, L. Biferale, G. Boffetta, A. Celani, M. Cencini, A. Lanotte, S. Musacchio, and F. Toschi, "Acceleration statistics of heavy particles in turbulence," J. Fluid Mech. **550**, 349 (2006).
[74]B. Viggiano, T. Basset, S. Solovitz, T. Barois, M. Gibert, N. Mordant, L. Chevillard, R. Volk, M. Bourgoin, R. B. Cal *et al.*, "Lagrangian diffusion properties of a free shear turbulent jet," J. Fluid Mech. **918**, A25 (2021).
[75]J. Berg, S. Ott, J. Mann, and B. Lüthi, "Experimental investigation of Lagrangian structure functions in turbulence," Phys. Rev. E **80**, 026316 (2009).
[76]L. Bourouiba, "The fluid dynamics of disease transmission," Annu. Rev. Fluid Mech. **53**, 473–508 (2021).
[77]B. Hejazi, O. Schlenczek, B. Thiede, G. Bagheri, and E. Bodenschatz, "On the risk of infection by infectious aerosols in large indoor spaces," Aerosol Air Qual. Res. **22**, 220117 (2022).
[78]P. Bourrianne, N. Xue, J. Nunes, M. Abkarian, and H. A. Stone, "Quantifying the effect of a mask on expiratory flows," Phys. Rev. Fluids **6**, 110511 (2021).
[79]J. F. G. Schneiders and F. Scarano, "Dense velocity reconstruction from tomographic PTV with material derivatives," Exp. Fluids **57**, 139 (2016).
[80]S. Cai, Z. Wang, F. Fuest, Y. J. Jeon, C. Gray, and G. E. Karniadakis, "Flow over an espresso cup: Inferring 3-D velocity and pressure fields from tomographic background oriented Schlieren via physics-informed neural networks," J. Fluid Mech. **915**, A102 (2021).